Perovskite Thin Films via Atomic Layer Deposition

*Brandon R. Sutherland, Sjoerd Hoogland, Michael M. Adachi, Pongsakorn Kanjanaboos, Chris T. O. Wong, Jeffrey J. McDowell, Jixian Xu, Oleksandr Voznyy, Zhijun Ning, Arjan J. Houtepen, and Edward H. Sargent**

Deposited via facile fabrication methods from the solution or gas phase, $CH_3NH_3PbI_3$ is a direct-bandgap semiconductor with exceptional optoelectronic material properties.[1] It combines an optical bandgap in the near-infrared at 1.55 eV,[2] a remarkably high absorption per unit length exceeding 10^4 cm^{-1} just above the bandedge,[3,4] and charge carrier diffusion lengths up to and exceeding 1 μm.[4,5] The latter attests to a bandgap substantially free of charge-trapping defect states that are otherwise normally present in materials deposited under nonepitaxial growth conditions.[2]

Lead organohalide perovskites—$CH_3NH_3PbI_3$ and mixed-halide derivatives—have enabled great strides toward low-cost, high-efficiency photovoltaic cells, surging from solar cell power conversion efficiencies of 6.5%, to a certified 17.9% all in the short span of three years (Aug 2011–May 2014).[1–3,6–11] The impressive physical properties of this material have further been leveraged toward radiative devices: light-emitting diodes,[12] and lasers.[13–15] Perovskites are of increasing interest in light-emissive technology by virtue of their spectral tunability,[15] high photoluminescence (PL) yield,[13] long photogenerated carrier lifetimes,[13] and ambipolar charge transport.[4]

Lead-iodide perovskites are typically fabricated using one of three methods: (1) sequential deposition of solution processed PbI_2 followed by a solution[1] or gas phase[16] exposure to CH_3NH_3I, (2) directly from a lead-halide perovskite precursor solution,[2] or (3) through simultaneous coevaporation of a lead-halide salt and CH_3NH_3I.[9] These fabrication strategies have led to solid state thin films of high purity and crystallinity, resulting in a new class of efficient optoelectronic devices utilizing perovskites as an active medium.

Here, we pursued a perovskite fabrication strategy that would be compatible with conformal deposition by leveraging atomic layer deposition (ALD). ALD is a low-vacuum and low-temperature deposition technique with a wide process window capable of uniform, conformal growth of films over large areas with atomic thickness precision. Attractively, it is a proven technology, now adopted in the electronics industry in semiconductor manufacturing. Furthermore, ALD has demonstrated viability in high-throughput, roll-to-roll compatible processes, indicating its potential in manufacturing scale-up.[17]

Presently, there are no processes for the growth of halide compounds via ALD. Therefore, neither the direct growth of $CH_3NH_3PbI_3$ nor of PbI_2 for subsequent conversion to $CH_3NH_3PbI_3$, is available. To overcome this, we sought to deposit a seed layer to the formation of PbI_2, which could then be converted to $CH_3NH_3PbI_3$ thin films. Possible candidates with known ALD-enabled processes are PbO and PbS. We chose to pursue PbS since it has a lower bond dissociation energy ($D°_{PbS}$ = 3.3 eV, $D°_{PbO}$ = 4.1 eV)[18] and is thus more likely to react completely with reagents in subsequent processing. ALD of lead sulfide has yielded thin films with controlled thickness, high purity, and distinct crystallographic orientations.[19–21]

A chief benefit of ALD is its compatibility with a broad range of substrates by reason of strong adhesion under normal processing conditions. We chose glass due to its wide availability, its electrically insulating character, and its low refractive index, enabling relevant studies on the optical dynamics of the film. **Figure 1** details the perovskite ALD process. We begin with ALD of a seed film of lead sulfide from controlled alternating pulses of H_2S and $Pb(tmhd)_2$ ALD precursors. The glass substrate has been treated with O_2 plasma immediately prior to deposition for final cleaning and enhanced reactivity with H_2S due to increased hydroxyl surface passivation. Layers of PbS are grown with each cycle at a measured growth rate of 1.3 Å per cycle, ≈0.2 monolayers per cycle, consistent with prior reports.[19] Once the desired thickness of PbS has been grown, the entire film is then converted to PbI_2 through exposure to iodine gas generated by subliming solid iodine in a closed system. The PbI_2 is subsequently converted to $CH_3NH_3PbI_3$ ($MAPbI_3$) through a 60 s dip in methylammonium iodide (MAI) in IPA. This process is summarized in Figure 1a. Atomic force microscopy is used to measure the grain-size (D) and arithmetic mean roughness (R_a) of PbS, PbI_2, and $MAPbI_3$, as detailed in Figure 1b. All three films form polycrystalline domains with R_a and D values, respectively: PbS [1.8 nm, 30 ± 5 nm], PbI_2 [1.1 nm, 51 ± 8 nm], and $MAPbI_3$ [18.7 nm, 140 ± 80 nm]. The final $MAPbI_3$ perovskite film morphology is governed primarily by the MAI treatment. Insets show images of the films at each stage on a glass substrate after 330 cycles of ALD PbS (≈43 nm). The thicknesses of the PbI_2 and $MAPbI_3$ films were measured to be 40 and 75 nm, respectively. The film thicknesses at each stage are consistent with variations in the crystal lattice parameters of PbS ($a = c = 5.936$ Å, JCPDS 02–0699), PbI_2 ($a = 4.557$, $c = 6.979$ Å, JCPDS 07-0235), and $CH_3NH_3PbI_3$ (a = 8.78 Å, c = 12.70 Å, ref.[22]). Assuming random crystal orientations across a lateral

B. R. Sutherland, Dr. S. Hoogland, Dr. M. M. Adachi, Dr. P. Kanjanaboos, C. T. O. Wong, Dr. J. J. McDowell, J. Xu, Dr. O. Voznyy, Dr. Z. Ning, Prof. E. H. Sargent
Department of Electrical and Computer Engineering
University of Toronto
10 King's College Road, Toronto, Ontario M5S 3G4, Canada
E-mail: ted.sargent@utoronto.ca
Prof. A. J. Houtepen
Department of Chemical Engineering
Delft University of Technology
Julianalaan 136, 2628 BL Delft, The Netherlands

DOI: 10.1002/adma.201403965

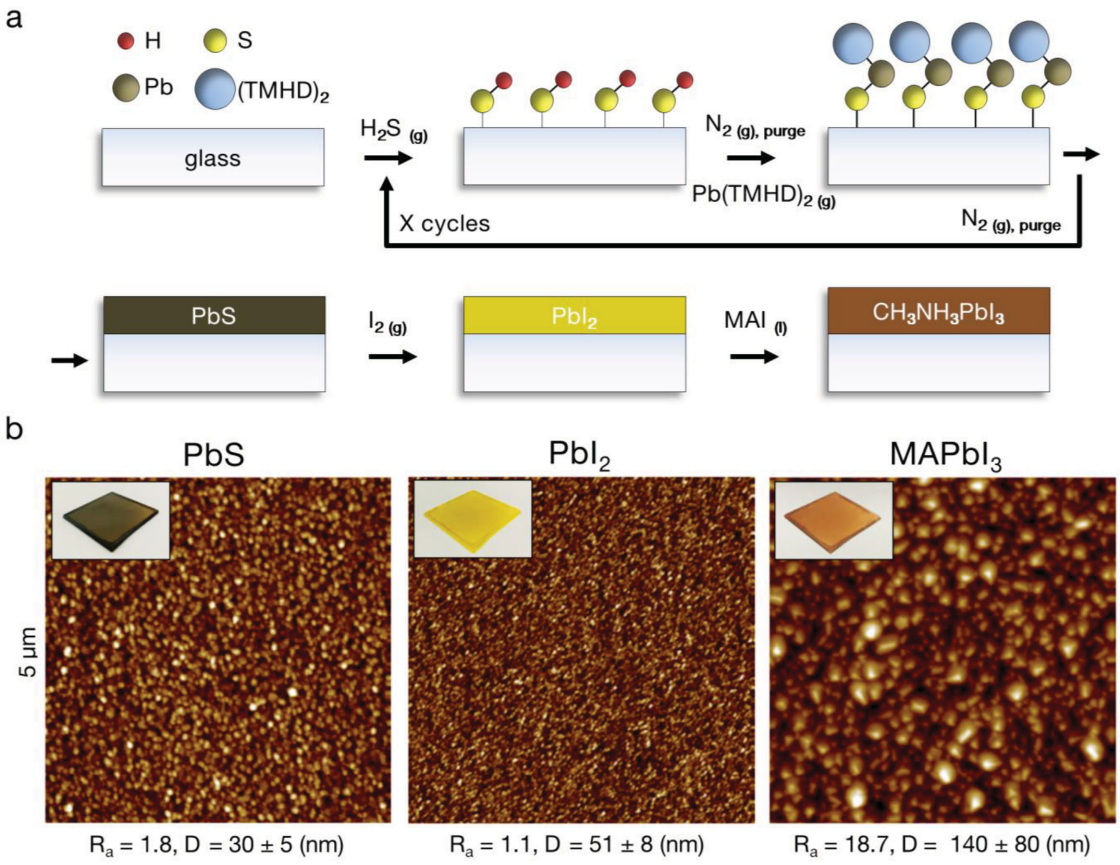

Figure 1. Perovskite ALD. a) Atomic layer deposition of $CH_3NH_3PbI_3$. ALD PbS is deposited from alternating cycles of H_2S and $Pb(tmhd)_2$ vapor on a glass substrate. The PbS sample is sealed in a nitrogen-atmosphere closed system with iodine chips sublimated at 120 °C to generate $I_{2(g)}$, converting the film to PbI_2. The PbI_2 films are dipped in CH_3NH_3I in IPA, resulting in full conversion to $MAPbI_3$. b) Atomic force microscopy study. 5 × 5 μm^2 windows are scanned to study the surface topology development during material processing. The arithmetic mean roughness, R_a, and the mean grain size, D, are shown below each image.

micron-scale (over which thickness is sampled via profilometry), the average lattice constants are: PbS: 5.936 Å, PbI_2: 5.768 Å, and $CH_3NH_3PbI_3$: 10.74 Å. For each film, the ratio of the averaged lattice constant, a_{avg}, to film thickness, d, are in excellent agreement, supporting the expectation of a complete place-exchange, with a_{avg}/d for PbS, PbI_2, and $CH_3NH_3PbI_3$: 72.4 ± 3.03, 69.3 ± 1.91, and 69.8 ± 17.4, respectively.

In **Figure 2**, we examine the spectroscopic properties of the thin films in the perovskite ALD process to determine their chemical makeup, confirm complete stepwise conversion, and assess their phase purity. X-ray photoelectron spectroscopy confirms the elemental presence of Pb, I, S, and N in each of the expected films: PbS, PbI_2, and $MAPbI_3$ (Figure 2a).

Through a complementary X-ray diffraction (XRD) analysis, we further confirmed the material composition at each step and demonstrated that the conversion processes of PbS to PbI_2, and PbI_2 to $MAPbI_3$, is complete, with no signatures of prior crystalline phases in subsequent films. Figure 2b correlates the measured XRD spectrum for the films at each step of the conversion process to the literature standards for PbS (JCPDS 02–0699), PbI_2 (JCPDS 07-0235), and $MAPbI_3$ (refs. [1,9,10,23]). ALD PbS shows one dominant (200) phase, and one secondary (400) peak (Figure 2b, bottom). After I_2 gas exposure, these peaks are no longer present, and characteristic hematite PbI_2 (001), (101), (003), and (004) signatures emerge. Following the treatment with MAI all previous peaks are absent and characteristic $MAPbI_3$ signatures appear: dominant (110) and (220) peaks, with a smaller (202) peak, and residual signatures of (312), (224), and (314). This confirms that the materials at each step of the perovskite ALD process are as designed and that the stepwise conversion produces a complete place-exchange.

A 45° scanning electron microscope image shows the polycrystalline grains on the surface of the fabricated $MAPbI_3$ films (**Figure 3**a). The spectral absorption coefficient, $\alpha(E)$ is shown in Figure 3b. The fabricated perovskite thin films have an absorption onset at 1.55 eV, with α, estimated from the measured optical density, exceeding 1.75 × 10^4 ± 830 cm^{-1} at the absorption knee at 1.66 eV, comparable to values reported in high-performance photovoltaic $MAPbI_3$ active layers.[4,11] The temperature-dependent PL is shown in Figure 3c. The room-temperature PL is centered at 1.63 eV, and decreases with decreasing temperature. A phase change from tetragonal to orthorhombic occurs between 150 and 125 K, after which the bandgap-temperature coefficient also changes from positive to negative, consistent with prior reports.[24]

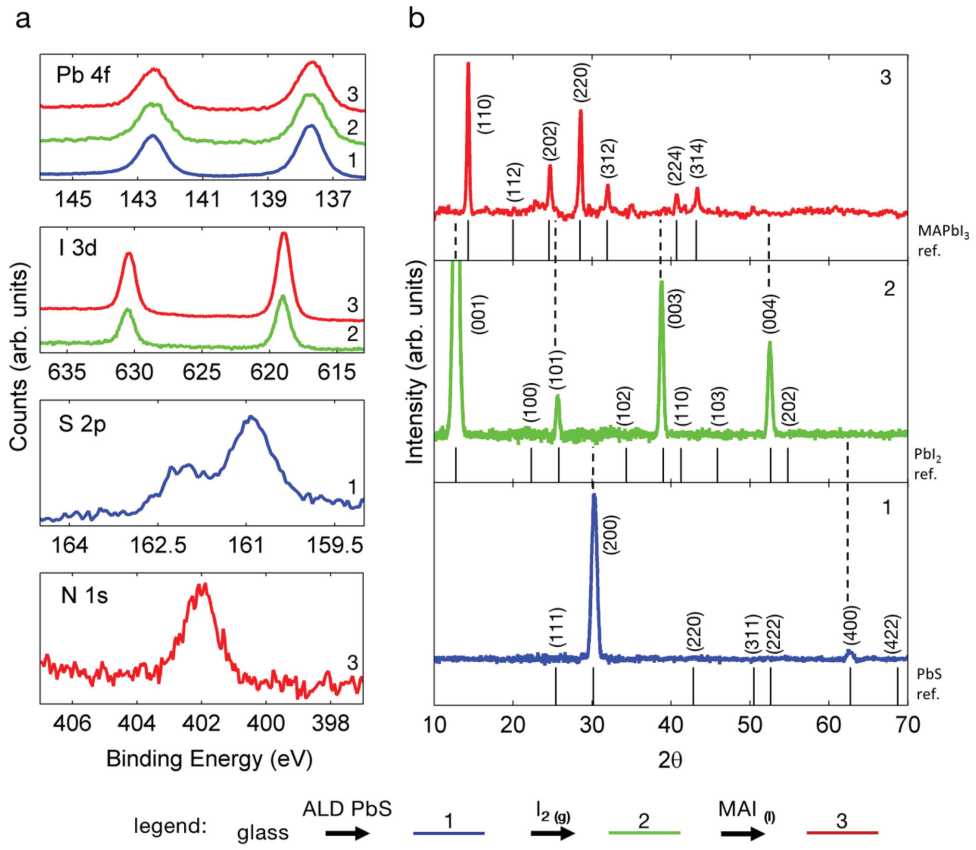

Figure 2. Material spectroscopy on the ALD perovskite process. a) X-ray photoelectron spectroscopic analysis. Pb4f signatures are observed in all films, I3d is present in PbI_2 and $MAPbI_3$, S2p is present in PbS, and N1s is present in $MAPbI_3$. b) X-ray diffraction analysis. The presence of expected crystallographic planes relative to the material references confirms the material at each stage of the ALD perovskite process. Furthermore, no prior crystal phases are present in subsequent films after processing from PbS to PbI_2 to $MAPbI_3$.

To elucidate gain dynamics, we studied the transient evolution of the film absorption using ultrafast pump-probe spectroscopy. We excited our sample with an optical pump of energy 2.70 eV, with 180 fs pulses at a repetition rate of 2.5 kHz, and probed the absorption with a white light source spanning 1.38–2.75 eV.

A representative 2D map of the transient absorption spectrum is shown in **Figure 4**a. Here, the change in absorbance ΔA is shown as a color height-map as a function of wavelength and delay time. The excitation fluence was 4.5 μJ cm^{-2}. Broad photoinduced absorption is observed between 500 and 700 nm. A short-lived derivative-like feature near the optical bandgap (see blue–red transition 750–790 nm in the first picosecond) indicates an excitation-induced redshift of the bandgap during the first few hundred femtoseconds. The most prominent feature is a strong absorption bleach near the bandgap that results from state-filling. For this relatively low fluence, the absorption bleach is long-lived.

To investigate material gain we focus on the total absorbance $A(E,t) = \Delta A(E,t) + A_0(E)$, where $A_0(E)$ is the linear absorption spectrum. Material gain is achieved when a negative total absorbance is observed. Figure 4b shows total absorption spectra at various pump-probe delay times obtained at a pump fluence of 70 μJ cm^{-2}. Gain is observed between ≈1.5 and 1.6 eV and shows a maximum at a pump-probe delay time of ≈3 ps, after which it decays.

To assess the spectral position of the maximum gain as a function of fluence, we show (Figure 4c) the total absorption spectrum at a 3-ps time delay for various excitation fluences. Figure 4d shows the time evolution of the absorbance plotted at the dotted line in Figure 4c at 1.58 eV, a photon energy just above the gain maximum. At fluences well above the gain threshold (36 and 70 μJ cm^{-2}), gain is seen to last as long as 200 ps.

At the lowest fluence, the decay of the absorption back to the linear absorption level is well-described by a single exponential with a 2-ns lifetime, in line with PL lifetimes previously published for lead-iodide perovskites.[13] At higher fluences, the decay becomes increasingly rapid, indicative of higher order recombination.

The inset in Figure 4d shows the minimum absorbance value (i.e., maximum gain) as a function of fluence, together with a third-order polynomial fit as a guide for the eye. A gain threshold of ≈16 μJ cm^{-2} is obtained. The maximum observed gain has a value of 10 mOD, together with the measured film thickness of this sample of 72 nm, this corresponds to a gain coefficient of 3200 ± 830 cm^{-1}. This value is comparable to single-crystal semiconductors used in commercial optical

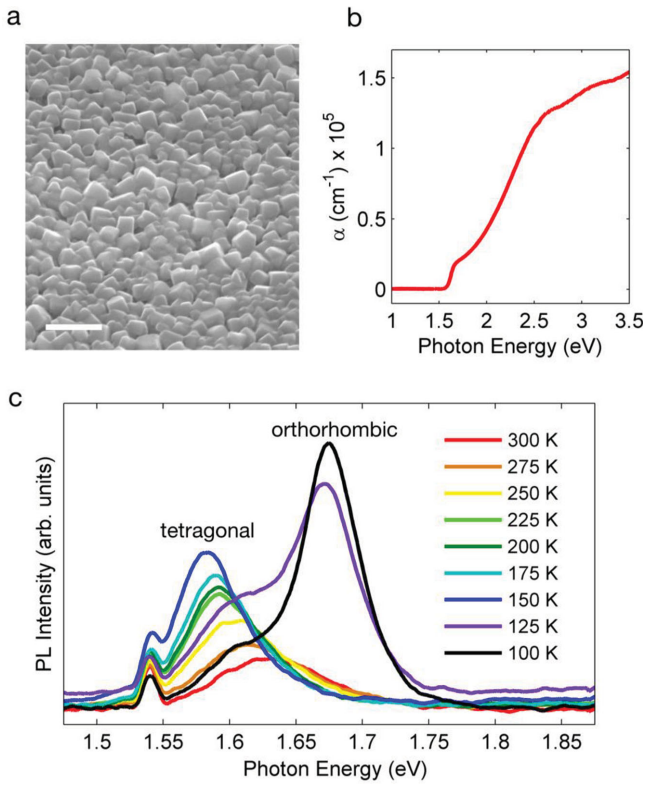

Figure 3. SEM, absorption, and photoluminescence of ALD perovskite thin films. a) A 45° SEM image of an ALD perovskite film. Scale bar is 200 nm. b) Absorption coefficient, α, of ALD perovskite films. The absorption onset is at 1.55 eV and α exceeds 10^4 cm^{-1} at the absorption knee at 1.66 eV, indicative of a strongly absorbing, high-quality perovskite film. c) Temperature-dependent photoluminescence shows a dominantly tetragonal room-temperature phase with a phase transition to orthorhombic between 150 and 125 K. The spectral feature at 1.54 eV is an unfiltered harmonic of the pump laser.

amplification technology.[25] This is, once again, a testament to the well-defined band edges of the perovskite film, despite the fact that it is a polycrystalline material.

Organometallic perovskite ALD is a versatile process for the deposition of perovskite thin films possessing exceptional materials quality for applications in next-generation optoelectronics. In particular, the impressive optical gain coefficient further highlights the potential for perovskites broadly in semiconductor-optical amplifiers and lasers. Utilizing perovskite ALD, facile and conformal integration of perovskites into a CMOS defined optical framework containing rib-waveguides and on-chip cavities such as elliptical and spherical resonators can be achieved. ALD for low-temperature, conformal, large-area growth of perovskites across a wide process-window offers promise in light emission and beyond.

Experimental Section

ALD Perovskite Sample Fabrication: Glass substrates were prepared by first sonicating in acetone, then isopropyl alcohol, and then deionized water, each for 15 min. Samples were exposed to a 10 min 100 mTorr oxygen plasma treatment immediately prior to atomic layer deposition (ALD).

$CH_3NH_3PbI_3$ perovskite films have been fabricated on these substrates by a three-step method. (A) PbS deposition: Cleaned glass slides are placed into a Cambridge Savannah S100 ALD system with the sample chamber held at 150 °C. Alternating pulses of $Pb(tmhd)_2$ and H_2S precursors (0.5 s pulse duration for both) build up the PbS film of a desired thickness. The purge time between precursor pulses was 20 s, and a nitrogen carrier gas was used at a volumetric flow rate of 10 sccm. (B) PbI_2 conversion: 100 mg of iodine chips are placed into a 250-mL container, which contains the ALD PbS films. The container is sealed in nitrogen and heated on a 120 °C hotplate for 16 h. After treatment, the samples are completely yellow and have been converted to PbI_2. (C) $MAPbI_3$ conversion: The PbI_2 films are dipped into a 30 mg mL^{-1} solution of CH_3NH_3I dissolved in isopropyl alcohol (IPA) for 60 s, immediately dipped into IPA for another 60 s, and then dried on a hot plate at 70 °C for 30 min.

Atomic Force Microscopy (AFM): AFM measurements were performed using PeakForce Tapping and PeakForce Quantitative Nanomechanical Property Mapping on Bruker Catalyst. Fast force curves were performed as the AFM scanned the samples' surfaces. Prior to measurement, the cantilever tip's radius and reflection sensitivity were measured via imaging on a rough surface and a force curve measurement on a quartz standard. In addition, the spring constant was measured via a thermal vibration measurement. Sharp cantilevers with tip radius smaller than 10 nm were used.

X-Ray Photoelectron Spectroscopy: A PHI-5500 XPS system was used to confirm the incorporation of Pb, I, S, and N in PbS, PbI_2, and $CH_3NH_3PbI_3$. A monochromated Al $K\alpha$ radiation source (1486.7 eV) was used to excite photoelectrons under ultrahigh vacuum.

X-Ray Diffraction (XRD): Phase purity was confirmed by powder XRD patterns collected with a Rigaku Miniflex diffractometer equipped with a Cu $K\alpha$ X-ray tube operated at 40 kV and 15 mA with a time per step of 3 s. Samples were rotated during data collection. Under these conditions, the intensity of the strongest reflection was approximately 1000 counts.

Scanning Electron Microscopy (SEM): A FEI Quanta FEG 250 environmental-SEM at an accelerating voltage of 10 kV, a working distance of 10 mm, and a pressure of 6.3×10^{-4} Pa was used sample imaging.

Absorption Coefficient: The optical density, A_{OD}, of the perovskite film was measured with a Perkin Elmer Lambda 950 spectrophotometer with an integrating sphere. A DekTak 3 profilometer was used to measure the film thickness, d. This was used to estimate the absorption coefficient, $\alpha = \log_{10}(e) \cdot A_{OD}/d$. Uncertainty was estimated from the measured surface roughness of the film.

Photoluminescence: Perovskite samples were excited with a frequency-tripled Nd:YAG 355 nm laser with a pulse duration of 2 ns and a repetition rate of 100 Hz. Photoluminescence was collected with an Ocean Optics USB 2000+ spectrometer. Samples were cooled to cryogenic temperatures using a home-built liquid nitrogen cryostat.

Ultrafast Pump-Probe Spectroscopy: A Light Conversion Pharos laser with an optical parametric amplifier (Orpheus, Lightconversion) and a Helios white-light transient absorption spectrometer from Ultrafast Systems were used for pump-probe measurements. The pump beam was a 460-nm laser source with 180 fs pulse duration and 2.5 kHz repetition rate. Transient absorption spectra in the visible (450–900 nm) were recorded with an Ultrafast Systems HELIOS spectrometer at a repetition rate of 5000 Hz using broadband probe pulses generated in a sapphire crystal pumped by the 1030 nm fundamental of the laser. The sample was held in an air-tight N_2-filled cell. To correct for chirp on the probe pulse, a bare glass substrate was measured. The time-zero was determined for each wavelength based on the coherent artifact. We subtracted a third-order polynomial fit to this coherent artifact from the raw data to obtain the chirp-corrected image shown in Figure 4a.

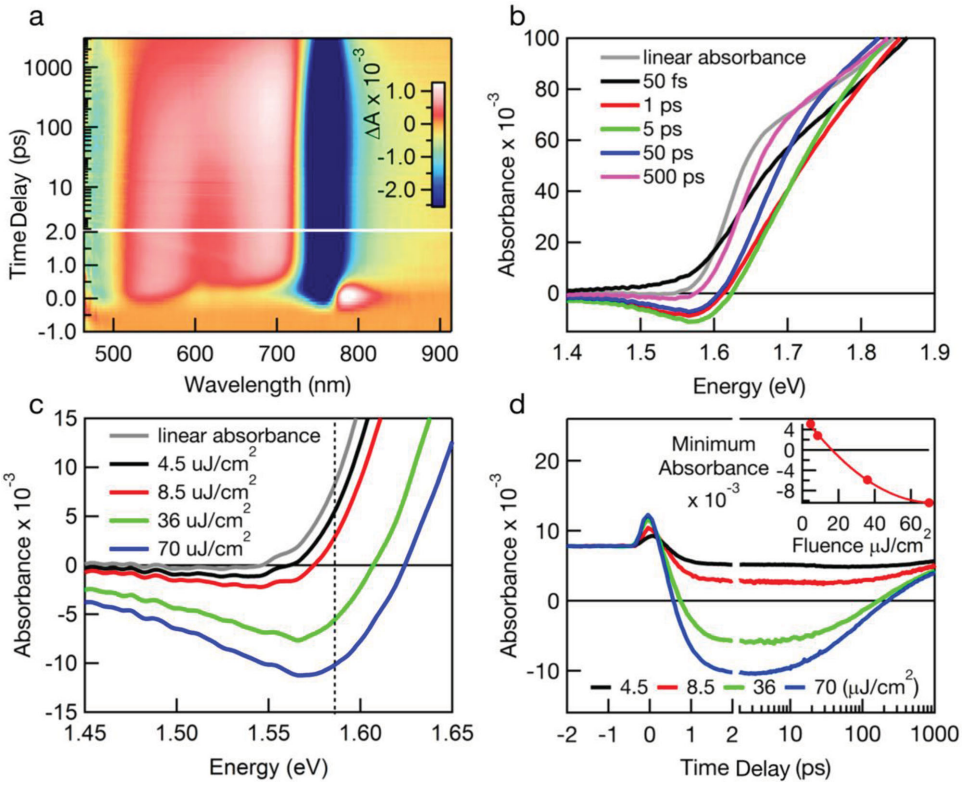

Figure 4. Ultrafast transient absorption measurements on ALD perovskites. a) 2D transient absorption image displaying the change in absorption (color-map) versus wavelength and time delay. The measurement was obtained with 460 nm pump pulses at a fluence of 4.5 μJ cm^{-2}. b) Nonlinear absorption spectra obtained at a fluence of 70 μJ cm^{-2}. Gain (negative absorbance) appears after 500 fs, reaches a maximum around 3 ps and subsequently decays, disappearing after 500 ps. c) Gain spectra at 3 ps (the time delay of maximum absorption bleach) for various fluences. For high photon fluence, gain with a large bandwidth is observed. d) Time-dependent nonlinear absorption plotted at just above the gain maximum (dotted line in (c) at 1.58 eV) for various fluences. At this energy, the two highest fluences exhibit gain over a period of 200 ps. The inset shows the minimum absorption versus fluence. The red solid line is a third-order polynomial fit that serves to guide the eye. A measured gain threshold of ≈16 μJ cm^{-2}, and an optical gain coefficient of 3200 ± 830 cm^{-1} are observed at 1.58 eV.

Acknowledgements

This publication is based in part on work supported by an award (KUS-11-009-21) from the King Abdullah University of Science and Technology (KAUST), by the Ontario Research Fund Research Excellence Program and by the Natural Sciences and Engineering Research Council (NSERC) of Canada. The authors thank Cambridge Nanotech, Fritz Prinz, and Orlando Trejo for their advice on ALD PbS film fabrication. The authors thank L.T. Kunneman for his assistance in the data analysis of the transient absorption measurements. The authors also thank M. Yuan, H. Dong, R. Wolowiec, and D. Kopilovic for their help during the course of the study.

Received: August 28, 2014
Published online: October 30, 2014

[1] J. Burschka, N. Pellet, S.-J. Moon, R. Humphry-Baker, P. Gao, M. K. Nazeeruddin, M. Grätzel, *Nature* **2013**, *499*, 316.
[2] M. M. Lee, J. Teuscher, T. Miyasaka, T. N. Murakami, H. J. Snaith, *Science* **2012**, *338*, 643.
[3] H.-S. Kim, C.-R. Lee, J.-H. Im, K.-B. Lee, T. Moehl, A. Marchioro, S.-J. Moon, R. Humphry-Baker, J.-H. Yum, J. E. Moser, M. Grätzel, N.-G. Park, *Sci. Rep.* **2012**, *2*, 1.
[4] G. Xing, N. Mathews, S. Sun, S. S. Lim, Y. M. Lam, M. Gratzel, S. Mhaisalkar, T. C. Sum, *Science* **2013**, *342*, 344.
[5] S. D. Stranks, G. E. Eperon, G. Grancini, C. Menelaou, M. J. P. Alcocer, T. Leijtens, L. M. Herz, A. Petrozza, H. J. Snaith, *Science* **2013**, *342*, 341.
[6] J.-H. Im, C.-R. Lee, J.-W. Lee, S.-W. Park, N.-G. Park, *Nanoscale* **2011**, *3*, 4088.
[7] J. H. Noh, S. H. Im, J. H. Heo, T. N. Mandal, S. I. Seok, *Nano Lett.* **2013**, *13*, 1764.
[8] J. H. Heo, S. H. Im, J. H. Noh, T. N. Mandal, C.-S. Lim, J. A. Chang, Y. H. Lee, H. Kim, A. Sarkar, M. K. Nazeeruddin, M. Grätzel, S. I. Seok, *Nat. Photonics* **2013**, *7*, 486.
[9] M. Liu, M. B. Johnston, H. J. Snaith, *Nature* **2013**, *501*, 395.
[10] N. J. Jeon, J. H. Noh, Y. C. Kim, W. S. Yang, S. Ryu, S. I. Seok, *Nat. Mater.* **2014**, *13*, 897.
[11] M. A. Green, A. Ho-Baillie, H. J. Snaith, *Nat. Photonics* **2014**, *8*, 506.
[12] Z.-K. Tan, R. S. Moghaddam, M. L. Lai, P. Docampo, R. Higler, F. Deschler, M. Price, A. Sadhanala, L. M. Pazos, D. Credgington, F. Hanusch, T. Bein, H. J. Snaith, R. H. Friend, *Nat. Nanotechnol.* **2014**, *9*, 687.
[13] F. Deschler, M. Price, S. Pathak, L. E. Klintberg, D.-D. Jarausch, R. Higler, S. Hüttner, T. Leijtens, S. D. Stranks, H. J. Snaith, M. Atatüre, R. T. Phillips, R. H. Friend, *J. Phys. Chem. Lett.* **2014**, *5*, 1421.
[14] Q. Zhang, S. T. Ha, X. Liu, T. C. Sum, Q. Xiong, *Nano Lett.* **2014**, *14*, 5995.

[15] G. Xing, N. Mathews, S. S. Lim, N. Yantara, X. Liu, D. Sabba, M. Grätzel, S. Mhaisalkar, T. C. Sum, *Nat. Mater.* **2014**, *13*, 476.
[16] Q. Chen, H. Zhou, Z. Hong, S. Luo, H.-S. Duan, H.-H. Wang, Y. Liu, G. Li, Y. Yang, *J. Am. Chem. Soc.* **2014**, *136*, 622.
[17] P. Poodt, V. Tiba, F. Werner, J. Schmidt, A. Vermeer, F. Roozeboom, *J. Electrochem. Soc.* **2011**, *158*, H937.
[18] K. Krane, *Modern Physics*, Wiley, New York/Chichester, UK, **2012**.
[19] N. P. Dasgupta, S. P. Walch, F. Prinz, *ECS Trans.* **2008**, *16*, 29.
[20] N. P. Dasgupta, W. Lee, F. B. Prinz, *Chem. Mater.* **2009**, *21*, 3973.
[21] N. P. Dasgupta, H. J. Jung, O. Trejo, M. T. McDowell, A. Hryciw, M. Brongersma, R. Sinclair, F. B. Prinz, *Nano Lett.* **2011**, *11*, 934.
[22] P. Umari, E. Mosconi, F. De Angelis, *Sci. Rep.* **2014**, *4*, 4467.
[23] Z. Chen, H. Li, Y. Tang, X. Huang, D. Ho, C.-S. Lee, *Mater. Res. Express* **2014**, *1*, 015034.
[24] Y. Yamada, T. Nakamura, M. Endo, A. Wakamiya, Y. Kanemitsu, *Appl. Phys. Express* **2014**, *7*, 032302.
[25] M. Fermann, A. Galvanauskas, G. Sucha, *Ultrafast Lasers: Technology and Applications*, CRC Press, Boca Raton, FL, USA **2002**.